

Cite this: DOI: 00.0000/xxxxxxxxxx

Rate-independent hysteretic energy dissipation in collagen fibrils†

Robert Magerle,^a Paul Zech,^a Martin Dehnert,^a Alexandra Bendixen,^a and Andreas Otto^a

Received Date

Accepted Date

DOI: 00.0000/xxxxxxxxxx

Nanoindentation cycles measured with an atomic force microscope on hydrated collagen fibrils exhibit a rate-independent hysteresis with return point memory. This previously unknown energy dissipation mechanism describes in unified form elastoplastic indentation, capillary adhesion, and surface leveling at indentation velocities smaller than $1 \mu\text{s}^{-1}$, where viscous friction is negligible. A generic hysteresis model, based on force-distance data measured during one large approach-retract cycle, predicts the force (output) and the dissipated energy for arbitrary indentation trajectories (input). While both quantities are rate independent, they do depend nonlinearly on indentation history and on indentation amplitude.

1 Introduction

Collagen fibrils are the tensile-load bearing components in connective tissue such as skin, ligament, tendon, cartilage, and bone.¹ A tendon owes its remarkable tensile strength and bending flexibility to the molecular structure of type I collagen and the supramolecular order in collagen fibrils.² Type I collagen forms 300 nm long triple-helical protein assemblies (tropocollagens), which are staggered and aligned along the fibril's axis.³ This results in a smectic-like order with 67 nm repeat distance. This periodic D-band pattern is visible in electron microscopy^{4,5} and atomic force microscopy (AFM) images (Fig. 1a). In the plane perpendicular to the fibril axis, the tropocollagen order is best described as being of polycrystalline texture, comprising small crystalline domains ordered quasi-hexagonally.^{5,6}

Finding out how collagen molecules and fibrils respond to mechanical stress and how energy is dissipated are topics of current research, whose purpose it is to reveal the molecular mechanisms involved^{2,7–9} and to provide an understanding of the changes connective tissues undergo due to ageing and disease.^{10–13} To achieve this, AFM is used to image and measure mechanical properties of individual collagen fibrils in the hydrated state, either in buffer solution^{8,10,14–19} or in humid air.^{20–22} The hysteresis between force-distance (FD) data measured during tip approach and tip retraction (Fig. 1b) is commonly referred to as viscoelastic behavior,^{15,21} since it is similar to the behavior of much softer and more fluid-like biological matter.^{23,24} This implies that vis-

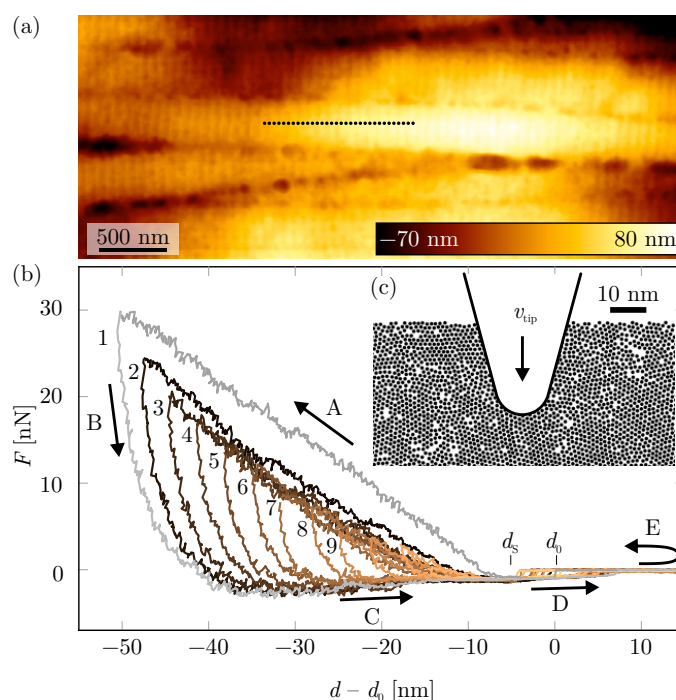


Fig. 1 Steady-state hysteresis in cyclic AFM nanoindentation measurements. (a) AFM height image of native hydrated collagen fibrils. (b) Cyclic measurements of the force F as a function of the tip-sample distance $d - d_0$ taken at an overlap position show steady-state hysteresis after the initial conditioning cycle (gray). Position d_0 is the onset of the capillary force, indents are enumerated. The indent is made in the radial direction, perpendicular to the fibril axis, with $v_{\text{tip}} = 0.05 \mu\text{s}^{-1}$. The measurements are made on the collagen fibril marked in (a). (c) Schematic cross-section perpendicular to the fibril axis at the tip apex (8 nm radius, 30° opening angle). Dots represent tropocollagen molecules.

^a Fakultät für Naturwissenschaften, Technische Universität Chemnitz, 09107 Chemnitz, Germany.

† Electronic Supplementary Information (ESI) available: Experimental protocol for cyclic FD measurements, additional FD data illustrating steady-state hysteresis, and dissipated energy measured in cyclic indentation experiments. See DOI: 10.1039/cXsm00000x/

cous friction is the main cause of energy dissipation and leads to the widespread assumption that the friction force is proportional to tip velocity v_{tip} .^{24–26}

Here, we report our finding that energy dissipation does in fact not depend on the indentation rate for $v_{\text{tip}} \leq 1 \mu\text{m s}^{-1}$ (Fig. 2). The nanoindentation response of hydrated collagen fibrils displays a rate-independent hysteresis with return point memory that depends only on the last return point. We find that the return points are the tip positions where the tip motion changes its direction. This energy dissipation mechanism dominates at slow deformation rates and cannot be captured with linear and quasilinear viscoelastic mechanical models²³ that are based on combinations of spring and dashpot elements.^{24,27,28}

Return point memory is a specific type of memory formation in hysteretic systems that allows the system to return to a previous state—the return point—at a later time.^{29,30} After a return point has been revisited and passed through again, the memory of that return point is wiped out. This is observed in ferromagnetic materials^{29,31} and in thermoelastic martensitic transformations of shape memory alloys.^{32,33} For further examples see ref. 29 and references therein. Return point memory is also found in the elastoplastic deformation of cast iron³⁴ and in cyclic nanoindentation of Fe-based amorphous alloys.³⁵ The analogy with the latter shows that hydrated type I collagen fibrils are soft, ductile solids with elastoplastic deformation behavior. This is in accordance with the finding that native type I collagen fibrils are in the glassy state at physiological conditions.³⁶ Collagen fibrils, however, are soft enough that the surface tension causes a capillary bridge to form and the surface to level out after the AFM tip is withdrawn.

What is more, we present a generic hysteresis model that describes in unified form sequences of the aforementioned distinct mechanical phenomena occurring in AFM-based nanoindentation experiments: elastoplastic indentation, capillary adhesion, and surface leveling (EPICAL). The model is based on measured FD data and it predicts the force (output) for arbitrary indentation trajectories (input) over a wide range of tip velocities and indentation amplitudes. This accurately predicts the dissipated energy. The model also accounts for attractive forces due to adhesion and the capillary interaction, which are known hysteretic energy dissipation mechanisms in AFM.^{37,38}

2 Results and discussion

2.1 AFM-based nanoindentation experiments

We study native collagen fibrils extracted from chicken tendon, deposited onto a polished Si wafer, and measured in humid air at 90% relative humidity (Fig. 1a). For details on materials and methods, see Appendix A. For each tip velocity, we measure cyclic FD data at increments of 32 nm along the crest of a single collagen fibril (indicated by black dots in Fig. 1a). This allows us to distinguish between the mechanical response of overlap regions and that of gap regions. We measure FD data by approaching the tip with a velocity v_{tip} until the maximal-force setpoint F_M is reached. From this point on, the tip is made to retract with the same velocity. Remaining in the same position, this is followed up

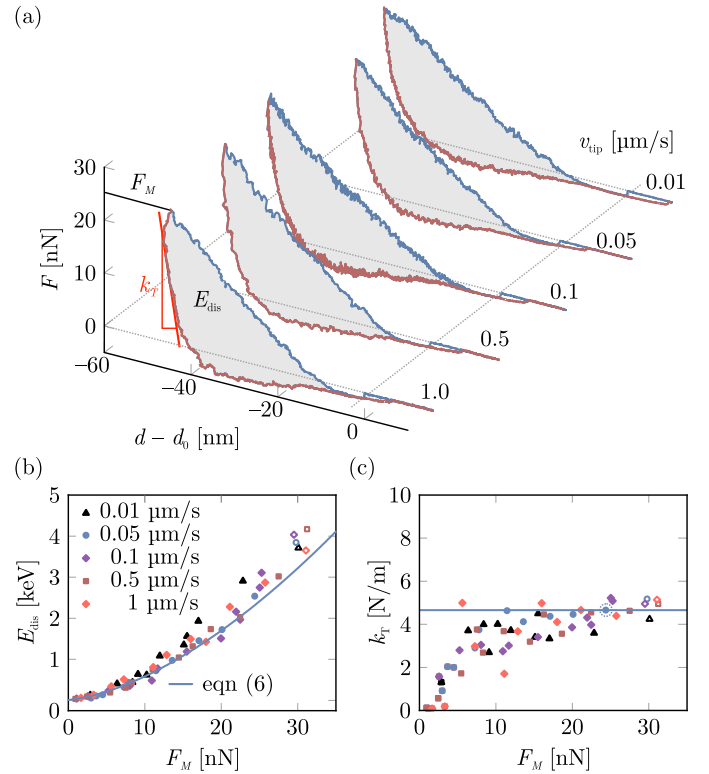


Fig. 2 Rate-independent energy dissipation. (a) FD data measured with different tip velocities v_{tip} during tip approach (blue) and tip retraction (red). The measurements are made on the collagen fibril marked in Fig. 1a. (b) E_{dis} as a function of F_M measured with different v_{tip} in cyclic indentation experiments. Data points with open symbols are from initial conditioning cycles. The curve is the prediction with the rate-independent hysteresis model for $v_{\text{tip}} = 0.05 \mu\text{m s}^{-1}$. (c) k_T as a function of F_M . The line and the circle indicate the value used in the hysteresis model's prediction shown in (b).

by repeated indentation cycles with an incrementally decreasing setpoint F_M (Fig. 1b). The temporal evolution of the corresponding force probing protocol is shown in Fig. S1†.

2.2 Steady-state hysteresis

In the following, we focus on the overlap regions. Gap regions display the same type of hysteresis behavior (data not shown) but are about 15% softer.^{16,22} The shape of the repulsive section of FD data (Figs. 1b and 2a) is typical for elastoplastic deformation, much like that occurring in nanoindentation experiments on glassy polymers,³⁹ inorganic solids,⁴⁰ and metallic glasses³⁵. On hydrated collagen fibrils, however, the remnant indentation is negligible ($< 1 \text{ nm}$). This counterintuitive effect is caused by surface tension, which we outline in greater detail. The first indentation–retraction cycle (gray line in Fig. 1b) initializes the tip–sample contact. All following indentation–retraction cycles share a common approach trajectory and a common retraction trajectory. This indicates steady-state hysteresis. Further evidence is provided by cyclic nanoindentation measurements performed with a constant maximal-force setpoint F_M that perfectly overlap (Fig. S2†).

During hysteresis, the following sequence of distinct mechani-

cal processes occurs, which we label with capital letters as shown in Fig. 1b: (A) Elastoplastic deformation during tip indentation. (B) Upon tip retraction, the force decreases due to the fibril's elastic response. (C) This is followed by a regime of attractive forces, caused by adhesion, by the capillary force, and by the formation of a capillary bridge. (D) Retracting the tip well beyond the original surface breaks the capillary bridge at d_{off} . (E) During further tip retraction and the following tip-approach period, the surface tension causes surface leveling. As a result, the onset of the capillary force occurs approximately at the same position d_0 for all indentation cycles. The overall behavior can be characterized as being shape reversible while being dissipative at the same time.

2.3 Energy dissipation

The shape of FD curves is independent of tip velocity in the range from 0.01 to $1\mu\text{ms}^{-1}$, as shown for FD data sets measured after the initial conditioning cycle (Fig. 2a). The energy dissipated during each approach-retract cycle, E_{dis} , is represented by the area enclosed between the FD data measured during tip approach and tip retraction (Fig. 2). By integrating we obtain E_{dis} as a function of the maximal-force setpoint F_M for every FD cycle. The dissipated energy E_{dis} is independent of v_{tip} and depends only on the maximal-force setpoint F_M (Fig. 2b). Figure 2b shows the data from cyclic nanoindentation experiments for each tip velocity. For each velocity, we repeated this measurement at multiple locations along the same collagen fibril. All E_{dis} data measured at the overlap regions are shown in Fig. S3† and display the same behavior as in Fig. 2b. For each tip velocity and F_M value, the scatter (standard deviation) of the E_{dis} data is typically below 20% (Fig. S3†).

2.4 Contact stiffness

We interpret the force decrease during a small tip retraction as the fibril's elastic response. This is evident in experiments with multiple small retract-approach cycles that are discussed in Section 2.6. We determine the contact stiffness k_T from the slope of FD data measured during tip retraction (Fig. 2a), which is comparable to the Oliver-Pharr method.⁴⁰ The computational procedure is detailed in Section 2.9. We find that the contact stiffness k_T is also independent of tip velocity. It increases only slightly for $F_M > 5\text{ nN}$ (Fig. 2c). In the hysteresis model, we use the k_T value obtained for the second indent measured with $v_{\text{tip}} = 0.05\mu\text{ms}^{-1}$, that represents the steady-state situation.

2.5 Repulsive forces

In our hysteresis model, we describe the repulsive forces phenomenologically with an algebraic function resembling the functional form of common contact models; see below, eqn (1a). The Hertz model as well as related contact models⁴¹ are only valid for elastic materials and cannot describe plastic deformation. Despite this limitation, the functional form of elastic models is frequently used for describing FD data beyond the elastic regime.^{21,22,24,27,28,42}

2.6 Return point memory

Experiments with more complex tip trajectories, including multiple intermediate retract-approach cycles (gray regions in Fig. 3a), clearly show rate-independent hysteretic behavior with return point memory. At the end of each intermediate retract-approach cycle the system returns to the starting point of each cycle ($1 \rightarrow 2 \rightarrow 1$, $3 \rightarrow 4 \rightarrow 3$, $5 \rightarrow 6 \rightarrow 5$, $7 \rightarrow 8 \rightarrow 7$ in Fig. 3b). This is a clear signature of the return point memory. Since no inner loops occur, the system state depends only on the last return point (Fig. 3a,b).

In our case, the return points are the positions d_i^* where the tip velocity changes its sign along with corresponding times t_i^* and $i = 1, \dots, N$ (Fig. 3). For a starting point well above the surface, an FD trajectory is uniquely determined by its sequence of return points, which carry the system's built-in memory. In Fig. 3, for instance, the return point $i = 3$ marks the start of an intermediate retract-approach cycle. After passing this point, the system enters an excursion, whereby the force starts to decrease linearly. During these intermediate excursions, the force changes approximately linearly (elastic). It has a contact stiffness similar to k_T (Fig. 2c). Before the return point $i = 3$, and after reaching this position again, the force increases with a power of d following the outer hysteresis loop. This corresponds to the FD data measured with a large indentation amplitude (Fig. 2).

2.7 Rate-dependent phenomena

Hysteresis is also observed for $v_{\text{tip}} > 1\mu\text{ms}^{-1}$, at which point a small phase lag between force (stress) and indentation (strain) causes the formation of inner hysteresis loops due to viscous friction (see Appendix B). In the studied velocity range, stress relaxation and creep progress more slowly than the tip velocity, which is why they do not influence the time evolution of $F(t)$ occurring during the measurement of FD data (see Appendix C).

2.8 Hysteresis model

Our aim is to produce a concise model that encompasses the following key features of the tip-sample interaction for arbitrary tip indentation trajectories: the repulsive force during initial tip indentation, the contact stiffness during intermediate retract-approach cycles, and the attractive force caused by adhesion and capillary bridge formation, followed by surface leveling.

The first step towards our goal is to present a hysteresis model with return point memory for the domain $d \leq d_0$. Then we add the elementary hysteresis for capillary bridge formation and its collapse in the domain $d > d_0$. For modeling, we introduce the dimensionless quantities force $f = F/1\text{ nN}$, distance $\delta = (d - d_0)/1\text{ nm}$, and time $\tau = t/1\text{ s}$.

For $\delta \leq 0$, we deduce a phenomenological hysteresis model based on the form of measured FD data by defining three time-independent functions that describe three characteristic regimes of the tip-sample interaction: $f_A(\delta)$ for the tip approach trajectory, $f_T(\delta, \delta_i^*)$ for the elastic response during intermediate retract-approach cycles, and $f_R(\delta)$ for the attractive-force limit of the re-

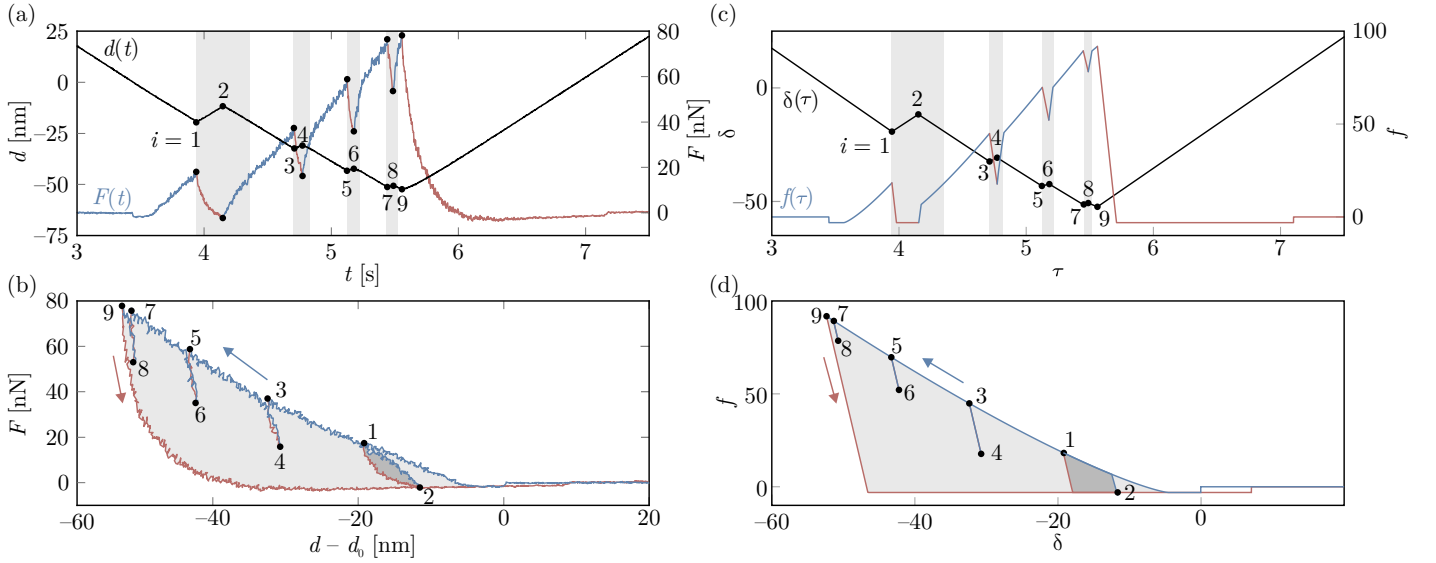


Fig. 3 Return point memory in indentation trajectories with multiple retract-approach cycles. Return points (●) are sequentially numbered. (a) Tip-sample distance $d(t)$ and force $F(t)$ measured between the AFM tip and a collagen fibril in humid air during an indentation trajectory involving several approach (blue) and retract periods (red) with $v_{\text{tip}} = 0.04 \mu\text{m s}^{-1}$. This measurement is made on an isolated collagen fibril deposited on a Si substrate. (b) Same F data plotted as a function of tip-sample distance $d - d_0$ which takes the cantilever bending into account. (c) Input $\delta(\tau)$ (thin line) determined from the measured indentation trajectory shown in (a) and the output $f(\tau)$ (thick line) calculated with the hysteresis model. (d) The same data plotted in the δ - f plane.

tract trajectories:

$$f_A(\delta) = \begin{cases} f_c, & \delta_s < \delta \\ \kappa_A(\delta_s - \delta)^\gamma + f_c, & \delta \leq \delta_s, \end{cases} \quad (1a)$$

$$f_T(\delta, \delta_i^*) = f(\delta_i^*) - \kappa_T(\delta - \delta_i^*), \quad (1b)$$

$$f_R(\delta) = f_c. \quad (1c)$$

Here, $\delta = \delta(\tau)$ is the actual input of the system at time τ , $\delta_i^* = \delta(\tau_i^*)$ is the last return point, f_c is the attractive (capillary) force, and δ_s the surface position. The function $f_A(\delta)$ resembles the functional form of common contact models.⁴¹ The parameter $\kappa_T = k_T/1\text{Nm}^{-1}$ is the dimensionless contact stiffness. The stiffness κ_A is determined by the tip's shape (radius and opening angle) and the sample's yield strength.

This describes the input-output diagram of the hysteresis model (Fig. 4). For $\delta < \delta_s$, and a given input δ , multiple output values f are possible within the transition region T; the trajectory taken is determined by the system's entry point into region T, that are return points of the input δ . Complex tip trajectories include multiple return points δ_i^* , which represent the system's memory. This memory is implemented by defining the output trajectory $f(\tau)$ piecewise between return points δ_i^* , which are the points where the tip velocity $dd/d\tau$ changes its sign along with the corresponding times τ_i^* and $i = 1, \dots, N$:

$$f(\tau) = \begin{cases} \min\{f_T(\delta, \delta_i^*), f_A(\delta)\}, & \delta - \delta_i^* < 0 \\ \max\{f_T(\delta, \delta_i^*), f_R(\delta)\}, & \delta - \delta_i^* > 0, \end{cases} \quad (2)$$

where $\delta = \delta(\tau)$, $\delta_i^* = \delta(\tau_i^*)$, and $\tau_i^* < \tau \leq \tau_{i+1}^*$. An equivalent, but

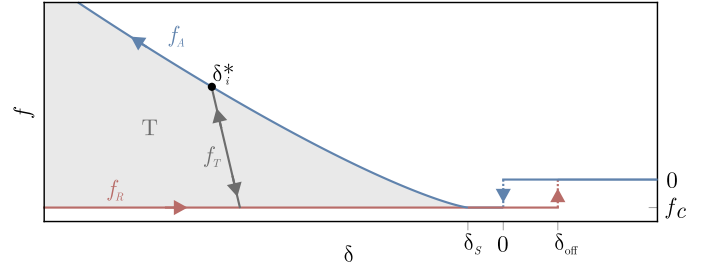


Fig. 4 Input-output diagram of the EPICAL hysteresis model. The multistable region T is enclosed by the functions $f_A(\delta)$ and $f_R(\delta)$ for $\delta \leq 0$. The function $f_T(\delta, \delta_i^*)$ describes the elastic response within the region T. The elementary hysteresis due to capillary bridge formation occurs for $0 < \delta < \delta_{\text{off}}$.

more compact form of eqn (2) is

$$\hat{\Gamma}[\delta](\tau) := f(\tau) = \max\left\{f_R(\delta), \min\{f_A(\delta), f_T(\delta, \delta_i^*)\}\right\}. \quad (3)$$

Equation (3) defines a hysteresis operator $\hat{\Gamma}[\delta]$ that acts on a whole input trajectory $\delta(\tau)$ and yields the output $f(\tau) = \hat{\Gamma}[\delta](\tau)$. For numerical computations eqn (2) can be understood as an iterative rule that determines the output $f(\tau)$ at time τ for an infinitesimally small indentation step $\Delta\delta = \delta(\tau) - \delta(\tau')$ from a given pair $(\delta(\tau'), f(\tau'))$ at time τ' . It should be noted that this rule, and the corresponding hysteresis operator $\hat{\Gamma}[\delta]$, are rate-independent given that eqns (2) and (3) do not depend on the time step $\Delta\tau = \tau - \tau'$.

The hysteresis model displays multistability for $\delta < \delta_s$ since, for a given input δ , a range of output values f are possible and the model displays return point memory only on the previous return point from the sequence of return points δ_i^* . In the region $0 < \delta <$

δ_{off} , capillary bridge formation, and its collapse, cause bistability which is described with an elementary hysteresis model.⁴³ For $\delta(\tau) \geq \delta_{\text{off}}$, the output is unique with $f(\tau) = 0$. In this regime, surface tension causes the leveling of the surface, and with it the system loses its memory.

The input–output behavior is summarized in Fig. 4. What is more, the hysteresis operator \hat{F} given by eqn (3) shows similarity to the generalized stop operator,^{44,45} which is a generalization of Prandtl’s model of elasto-plasticity.^{34,46–48} The generalized stop operator limits the output to a finite range of values. In our case, these limits are (1) the function f_A , which describes the maximal repulsive force due to the material’s yield strength, and (2) the function f_R , which describes the attractive force due to adhesion and the capillary force.

2.9 Comparison with experiments

The EPICAL hysteresis model highly accurately predicts the force and the dissipated energy for complex tip trajectories. For a given FD data set, measured with large indentation amplitude (as in Fig. 1b), we determine the parameters that describe the EPICAL hysteresis model by fitting functions corresponding to eqns (1a), (1b), and (3) to the measured data. To this end, we use MATLAB with the EzyFit 2.44 Toolbox⁴⁹ and proceed successively as follows.

1: For every FD curve, the baseline was adjusted with a sine fit to correct the deflection offset and the laser interference effects during the measurement. 2: The position d_0 , the onset of attractive forces, was determined as described in ref. 42 (Fig. 5a). 3: The capillary force F_C is set to the minimal force value within an FD data set measured during tip approach (Fig. 5a). The corresponding d position was used as a starting point for d_S in the following fitting step. 4: A power-law function $F_A(d)$ with offset F_C , which is analogous to eqn (1a), was fitted to the FD data measured during tip approach (blue curve in Fig. 5a). The maximum indentation $d_{\text{min},A}$ and F_C were kept fixed, whereas κ_A , γ and d_S were varied. Note, that the obtained parameters κ_A and γ are sensitively dependent on d_S . This is caused by the scale invariance of the power-law. It still remains that the resulting fitting function $F_A(d)$ is a good approximate description of the particular FD data set with an analytical function. 5: A power-law function

$$F_R(d) = k_R(d_{S,R} - d)^\beta + F(d_{S,R}) \quad (4)$$

that is analogous to $F_A(d)$ was fitted to the FD data measured during tip retraction (dashed curve in Fig. 5a) within the fitting range $d_{\text{min},R} < d < d_{S,R}$, where $d_{S,R}$ is the position of the smallest force value; k_R , $d_{S,R}$, and β were fitting parameters, while $F(d_{S,R})$ is kept fixed. From the resulting fit function, the contact stiffness k_T is obtained as the absolute value of the slope at $d_{\text{min},A}$

$$k_T = \left| -k_R \beta (d_{S,R} - d_{\text{min},A})^{\beta-1} \right|. \quad (5)$$

The dimensionless contact stiffness $\kappa_T = k_T / 1 \text{ Nm}^{-1}$.

Fitting parameters for selected data sets are shown in Table 1, which allow for the construction of the hysteresis operator according to eqns 1 and 3. An example for the force predicted with

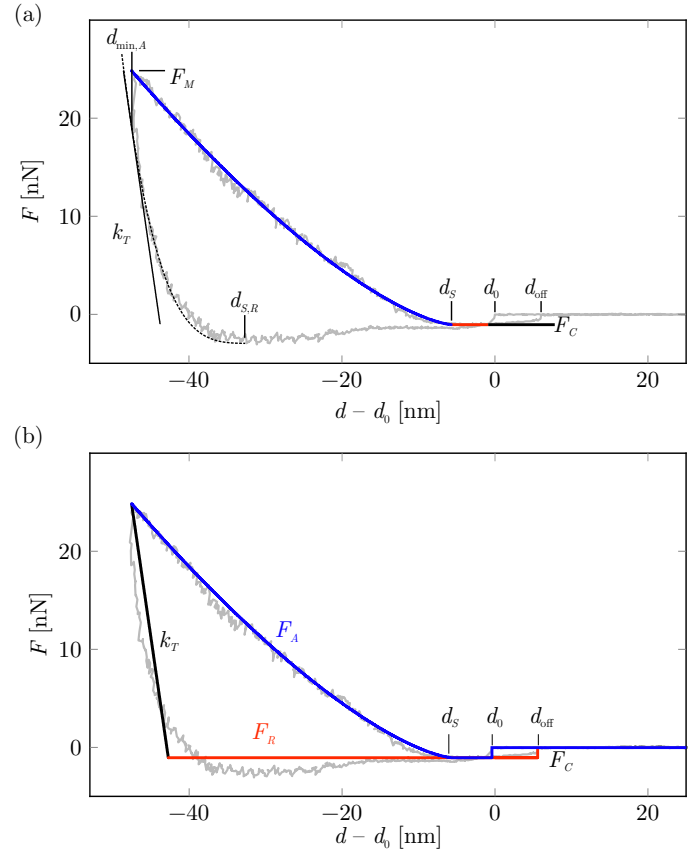


Fig. 5 (a) Piece-wise fitting procedure for obtaining the parameters describing the hysteresis operator. The FD data are measured on a collagen fibril within a bundle of many fibrils. (b) Force predicted with the hysteresis operator for the entire indentation cycle.

Table 1 Fit parameters in dimensionless units.

FD data set	Fig. 1b ^a	Fig. 1a ^b	Fig. 3
AFM cantilever	Type II	Type II	Type I
v_{tip}	$0.05 \mu\text{ms}^{-1}$	$0.05 \mu\text{ms}^{-1}$	$0.04 \mu\text{ms}^{-1}$
parameter	value	mean \pm SD	value
f_c	-1.08	-0.976 ± 0.161	-4.77
δ_s	-10.0	-6.56 ± 2.51	-4.62
κ_A	0.192	0.116 ± 0.083^c	0.728
γ	1.26	1.52 ± 0.211^c	1.25
κ_T	3.58	5.32 ± 0.589	16.4
f_M	22.8	25.0 ± 2.88	76.5

^aSecond indentation cycle of FD data shown in Fig. 1b. ^bSet of second indentation cycles measured at 15 overlap positions along the line marked in Fig. 1a. ^cNote, that the fitting parameters κ_A and γ are sensitively dependent on d_S . This causes the large SD.

the hysteresis operator for the entire indentation cycle is shown in Fig. 5b.

The obtained parameters d_0 , d_{off} , and f_c describe the capillary interaction, d_S , κ_A , and γ describe the elastoplastic indentation, and the contact stiffness κ_T describes the elastic response. For simplicity, we describe adhesion with f_c . This defines the hysteresis model for the particular FD data set making it possible to determine the output $f(\tau)$ for any other $\delta(\tau)$ trajectory, for example, the one shown in Fig. 3a. Proceeding on this basis, we determine

the sequence of return points δ_i^* from the measured trajectory $d(t)$, which yields the $\delta(\tau)$ trajectory shown in Fig. 3c. The resulting $f(\delta(\tau))$ trajectory (Fig. 3c,d) represents all essential features of the measured force trajectory $F(d)$. Differences are only observed for the first small retract-approach loop starting at t_1^* and the last retract period starting at t_0^* , since we assumed trajectories in region T to be linear functions.

2.10 Dissipated energy

The dissipated energy is also correctly predicted by the hysteresis model. It is given by the integral $\oint f(\delta) d\delta$ over an indentation cycle. For the indentation cycles with varying F_M (Fig. 2b) we obtain in reduced units:

$$E_{\text{dis}}(f_M) = \frac{(f_M - f_c)^{\frac{1}{\gamma}+1}}{(1+\gamma)\kappa_A^{1/\gamma}} - \frac{(f_M - f_c)^2}{2\kappa_T}, \quad (6)$$

where f_M corresponds to F_M . The first term is the energy invested during tip indentation and the second is the elastic energy regained during tip retraction. The resulting $E_{\text{dis}}(F_M)$ (solid line in Fig. 2b) does not depend on v_{tip} and it describes the measured data very accurately for the entire range of F_M . It should be noted, that eqn (6) is the result of a specific set of indentation cycles. It slightly underestimates the dissipated energy since, for simplicity's sake, the adhesion is being described with f_c .

In general, the energy dissipated during an indentation cycle depends not only on the actual indentation δ and the indentation amplitude, but also on the last return point. Put simply: for small retract-approach amplitudes, the response is elastic, whereas for larger amplitudes, energy is dissipated, provided $f(\tau)$ switches between the boundaries f_R (maximal tensile strength) and f_A (maximal compressive strength). The first small loop starting at t_1^* (Fig. 3) exemplifies this.

2.11 Discussion

Collagen fibrils have an anisotropic molecular structure and therefore anisotropic mechanical properties. The stress-strain behavior of single collagen fibrils when stretched along the fibril axis is investigated using special micro-electromechanical systems^{50–52} or by attaching single collagen fibrils to AFM cantilevers.^{53–55} Under cyclic loading, partial plastic deformation, steady-state hysteresis, and related energy dissipation are observed. These measurements primarily study the deformation and sliding of adjacent tropocollagen molecules along their longitudinal axis. Uniaxial stretching along the fibril axis is also the subject of recent molecular dynamics computer simulations.^{2,7,9,56} A specific question in these studies is how different types of crosslinks between adjacent tropocollagen molecules affect the mechanical behavior of collagen fibrils.

In AFM-based nanoindentation experiments, on the other hand, tropocollagen molecules are pushed apart perpendicular to their longitudinal axis and sheared against each other in the plane perpendicular to the fibril axis, as suggested by large-scale molecular dynamics simulations of the nanoindentation response of amorphous³⁵ and nanocrystalline metals.⁵⁷ We expect similar

processes to occur within the nanocrystalline domain structure of collagen fibrils. In addition, the tropocollagen helix structure may deform, as suggested by molecular dynamics simulations of tensile loading of collagen fibrils.⁷ The cohesive force between adjacent tropocollagen molecules plays an important role in both fundamental deformation modes, stretching along the fibril axis and shearing perpendicular to the fibril axis, but the two deformation modes are fundamentally different, so nanoindentation experiments cannot be directly compared to stretching along the fibril axis.

3 Conclusions

In AFM nanoindentation experiments on hydrated collagen fibrils, at slow deformation rates, energy is dissipated via a rate-independent hysteretic process with return point memory and negligible viscous friction. The fibril's shape-reversible yet dissipative response is caused by a combination of interactions between elastoplastic indentation, adhesion, capillary force, and surface tension, which all together cause surface leveling.

Native, hydrated type I collagen fibrils are in the glassy state.³⁶ At ambient temperature, they are above the glass-to-rubber transition^{16,36,58} (in the leathery regime⁵⁹). Indeed, glassy polymers³⁹ as well as inorganic⁴⁰ and metallic glasses³⁵ show elastoplastic behavior under cyclic loading and in nanoindentation experiments. The underlying molecular mechanisms are material specific, and a range of models have been developed to describe the elastoplastic behavior of amorphous materials,⁶⁰ including different types of soft matter. Therefore, we anticipate that the slow (glassy) molecular dynamics cause the observed hysteretic behavior, and we expect that rate-independent hysteretic energy dissipation can also be found in other types of soft condensed matter, including biological materials.

Author contributions

Robert Magerle: Conceptualization (equal); Funding acquisition (equal); Methodology (equal); Resources (lead); Supervision (lead); Formal analysis (supporting); Visualization (supporting); Writing – original draft (equal); Writing – review & editing (equal). **Paul Zech:** Data Curation (supporting); Formal analysis (lead); Investigation (equal); Methodology (equal); Software (equal); Visualization (supporting); Writing – original draft (equal); Writing – review & editing (equal). **Martin Dehnert:** Data Curation (lead); Formal analysis (supporting); Investigation (equal); Methodology (equal); Software (equal); Visualization (lead); Writing – original draft (equal); Writing – review & editing (equal). **Alexandra Bendixen:** Conceptualization (equal); Funding acquisition (equal); Supervision (supporting); Writing – original draft (supporting); Writing – review & editing (supporting). **Andreas Otto:** Conceptualization (equal); Methodology (equal); Writing – original draft (supporting); Writing – review & editing (supporting).

Conflicts of interest

The authors declare no competing interests.

Acknowledgements

We acknowledge funding from the Volkswagen Foundation (grants I/77476 and 93794) and the Deutsche Forschungsgemeinschaft (INST 270/152-1 FUGG). We thank G. Radons for discussions and N. Moore for proofreading.

Appendix

A Materials and methods

A.1 Sample preparation

Polished, 1 cm × 1 cm large Si substrates were cleaned in a 1:1 mixture of acetone/toluene and mounted on a heating plate (150 °C). Subsequently, residual organic contamination was removed with a CO₂ jet (Snowjet, Spraying Systems Co., USA). A chicken's calcaneus (Achilles) tendon was removed from a fresh chicken leg sourced from a local supermarket. A piece of about 2 mm in length was extracted and spread out onto a polished Si substrate. After drying, the specimen was washed three times with deionized water, air-dried, and rehydrated with humid air in the AFM. The samples contain regions with bundles of collagen fibrils as well as isolated collagen fibrils.

A.2 Atomic force microscopy

For AFM measurements, a NanoWizard II instrument (JPK Instruments AG, Berlin, Germany) was used in conjunction with two types of silicon cantilevers (see Table 2). These stiff cantilevers minimize the jump-to-contact related hysteresis in the force–distance (FD) data. Measurements on hydrated collagen fibrils were performed at room temperature with 88%–90% relative humidity (RH) using a lab-built setup similar to that used in ref. 20–22. The specimen was allowed to equilibrate for at least 40 min before AFM measurements were performed.

Table 2 AFM cantilevers and their characteristic parameters.

	Type I	Type II
Manufacturer	NanoWorld AG (Neuchâtel, Switzerland)	NANOSENSORS (Neuchâtel, Switzerland)
Model	NCH	PPP-NCSTR
Tip radius ^a	< 8 nm	< 7 nm
Half opening angle ^a	35°	15°
Backside coating	none	Al
Length ^a	125 μm	150 μm
Width ^a	30 μm	27 μm
Thickness ^a	4 μm	2.6 μm
Resonance frequency ^b	330 kHz, 354 kHz ^d	159 kHz
Quality factor ^b	439.4, 476.6 ⁴	210.9
Spring constant ^c	26.08 N m ⁻¹ , 23.18 N m ⁻¹ ^d	4.67 N m ⁻¹

^aAs specified by the manufacturer. ^bMeasured values.

^cDetermined as in ref. 61. ^dCantilever used for measuring stress relaxation and creep.

A.3 Force–distance measurements

In a first set of experiments (Series I), we studied an isolated collagen fibril deposited on a Si substrate using Type I cantilevers.

We measured FD data sets with multiple intermediate retract–approach cycles at 10 positions with 100 nm pixel distance along the fibril's crest, with tip velocities v_{tip} ranging from 0.01 to 4 μm s⁻¹. The resulting FD data are shown in Figs. 3, 6 and 7.

In a second set of experiments (Series II), we studied a collagen fibril within a bundle of many fibrils using a Type II cantilever. For each tip velocity, we measured rows of 32 FD data sets with 32 nm pixel distance along the fibril's crest within a pristine part of the same collagen fibril (shown in Fig. 1a). The corresponding FD data are shown in Figs. 1, 2 and 5.

B Complex contact stiffness

For larger tip velocities, viscous friction causes the formation of inner hysteresis loops (Fig. 6). This effect can be described with a complex contact stiffness $k_T^*(\omega)$ as a function of frequency ω corresponding to the collagen fibril's complex dynamic modulus.⁶²

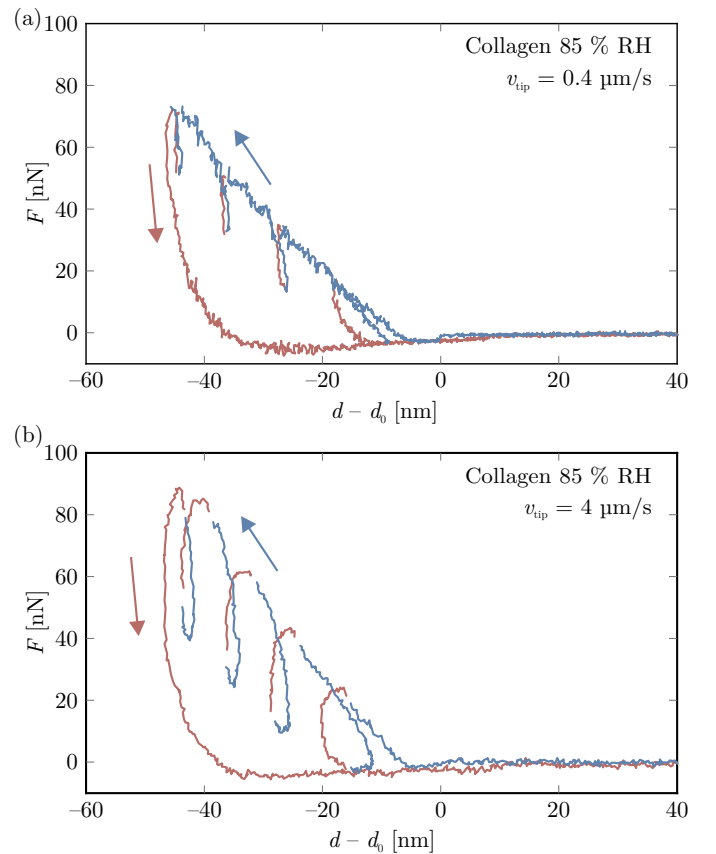


Fig. 6 Force trajectories with multiple retract–approach cycles measured on a hydrated collagen fibril using (a) $v_{\text{tip}} = 0.4 \mu\text{m s}^{-1}$ and (b) $v_{\text{tip}} = 4 \mu\text{m s}^{-1}$. The measurements are made on an isolated collagen fibril deposited on a Si substrate.

C Stress relaxation and creep

We measured stress relaxation and creep at the crest of isolated collagen fibrils deposited on a Si substrate at 85% RH using Type I cantilevers. For the stress relaxation measurement, the tip is made to indent with v_{tip} until a repulsive force of 100 nN is reached. Then, the tip position is held constant, at which time

the evolution of $F(t)$ is measured via the corresponding cantilever deflection $D(t)$ (Fig. 7a).

For measuring creep, the tip is indented until a repulsive force of 100 nN is reached. After this, the force is kept constant, and the tip indentation $Z - Z_0$ is monitored as a function of time (Fig. 7c). We obtain the initial deflection relaxation rate $\dot{D}_{\text{ini}} = [D(\Delta t) - D(0)]/\Delta t$ from the slope of $D(t)$ for $t \in [0, \Delta t]$, where $t = 0$ is the end of the tip approach period and Δt is indicated by the length of the slope shown as blue lines in Fig. 7a. The initial deflection relaxation rate \dot{D}_{ini} and the initial creep rate \dot{Z}_{ini} (determined analogously to \dot{D}_{ini}) are the upper boundaries for the relaxation rates (creep rates) during the stress relaxation (creep) experiment, as indicated with the dashed lines in Fig. 7b, d. Both stress relaxation and creep, proceed more slowly than the tip velocity and, therefore, do not influence the time evolution of $F(t)$ occurring during the measurement of FD data.

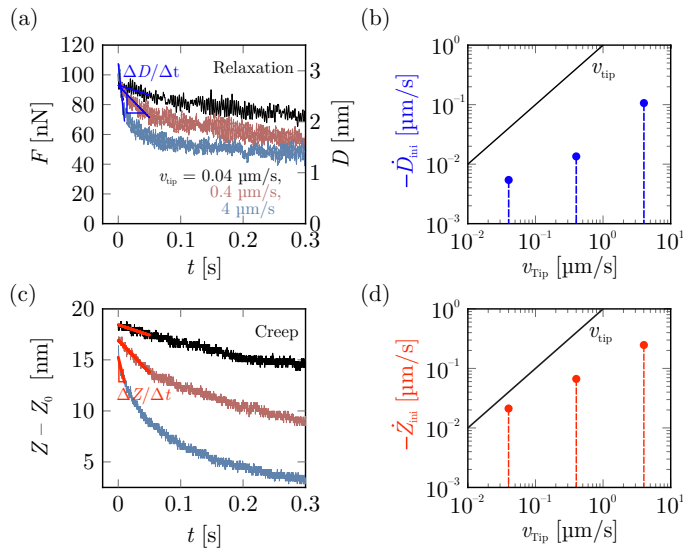


Fig. 7 Stress relaxation and creep are slower than tip velocity and do not affect FD data measured in cyclic indentation experiments. (a) Force relaxation $F(t)$ and the corresponding cantilever deflection $D(t)$ (solid lines) for different v_{tip} . (b) Initial deflection rate $-\dot{D}_{\text{ini}}$ as function of v_{tip} . (c) Creep $Z - Z_0$ for different v_{tip} . (d) Initial deflection rate $-\dot{Z}_{\text{ini}}$ as function of v_{tip} . The bisections $-\dot{D}_{\text{ini}} = v_{\text{tip}}$ and $-\dot{Z}_{\text{ini}} = v_{\text{tip}}$ are shown as black lines. The measurements are made on an isolated collagen fibril deposited on a Si substrate.

Notes and references

- 1 *Collagen: Structure and Mechanics*, ed. P. Fratzl, Springer US, 2008.
- 2 A. Gautieri, S. Vesentini, A. Redaelli and M. J. Buehler, *Nano Lett.*, 2011, **11**, 757–766.
- 3 J. P. R. O. Orgel, T. C. Irving, A. Miller and T. J. Wess, *Proc. Natl. Acad. Sci. U. S. A.*, 2006, **103**, 9001–9005.
- 4 D. W. L. Hukins and J. Woodhead-Galloway, *Mol. Cryst. Liq. Cryst.*, 1977, **41**, 33–39.
- 5 D. J. Hulmes, J. C. Jesior, A. Miller, C. Berthet-Colominas and C. Wolff, *Proc. Natl. Acad. Sci. U. S. A.*, 1981, **78**, 3567–3571.
- 6 D. Hulmes, T. Wess, D. Prockop and P. Fratzl, *Biophys. J.*, 1995, **68**, 1661–1670.

- 7 A. Masic, L. Bertinetti, R. Schuetz, S.-W. Chang, T. H. Metzger, M. J. Buehler and P. Fratzl, *Nat. Commun.*, 2015, **6**, 5942.
- 8 O. G. Andriotis, S. Desissaire and P. J. Thurner, *ACS Nano*, 2018, **12**, 3671–3680.
- 9 C. Zapp, A. Obarska-Kosinska, B. Rennekamp, M. Kurth, D. M. Hudson, D. Mercadante, U. Barayeu, T. P. Dick, V. Denysenkov, T. Prisner, M. Bennati, C. Daday, R. Kappl and F. Gräter, *Nat. Commun.*, 2020, **11**, 2315.
- 10 M. Stolz, R. Gottardi, R. Raiteri, S. Miot, I. Martin, R. Imer, U. Staufer, A. Raducanu, M. Düggelein, W. Baschong, A. U. Daniels, N. F. Friederich, A. Aszodi and U. Aebi, *Nat. Nanotechnol.*, 2009, **4**, 186–192.
- 11 A. D. Kemp, C. C. Harding, W. A. Cabral, J. C. Marini and J. M. Wallace, *J. Struct. Biol.*, 2012, **180**, 428–438.
- 12 A. D. Gonzalez, M. A. Gallant, D. B. Burr and J. M. Wallace, *J. Biomech.*, 2014, **47**, 681–6.
- 13 N. Chi, S. Lozo, R. A. Rathnayake, S. Botros-Brey, Y. Ma, M. Damaser and R. R. Wang, *Acta Biomater.*, 2022, **152**, 335–344.
- 14 M. Stolz, R. Raiteri, A. Daniels, M. R. VanLandingham, W. Baschong and U. Aebi, *Biophys. J.*, 2004, **86**, 3269–3283.
- 15 C. A. Grant, D. J. Brockwell, S. E. Radford and N. H. Thomson, *Biophys. J.*, 2009, **97**, 2985–2992.
- 16 S. J. Baldwin, A. S. Quigley, C. Clegg and L. Kreplak, *Biophys. J.*, 2014, **107**, 1794–1801.
- 17 O. G. Andriotis, P. J. Thurner, W. Manuyakorn, P. H. Howarth, D. E. Davies, J. Zekonyte, O. L. Katsamenis and S. Fabri, *J. Mech. Behav. Biomed.*, 2014, **39**, 9–26.
- 18 O. G. Andriotis, K. Elsayad, D. E. Smart, M. Nalbach, D. E. Davies and P. J. Thurner, *Biomed. Opt. Express*, 2019, **10**, 1841–1855.
- 19 O. G. Andriotis, M. Nalbach and P. J. Thurner, *Acta Biomater.*, 2023, **163**, 35–49.
- 20 E.-C. Spitzner, S. Röper, M. Zerson, A. Bernstein and R. Magerle, *ACS Nano*, 2015, **9**, 5683–5694.
- 21 M. R. Uhlig and R. Magerle, *Nanoscale*, 2017, **9**, 1244–1256.
- 22 R. Magerle, M. Dehnert, D. Voigt and A. Bernstein, *Anal. Chem.*, 2020, **92**, 8741–8749.
- 23 Y.-C. Fung, *Biomechanics*, Springer New York, New York, NY, 1993.
- 24 Y. M. Efremov, T. Okajima and A. Raman, *Soft Matter*, 2020, **16**, 64–81.
- 25 R. Garcia, C. J. Gómez, N. F. Martinez, S. Patil, C. Dietz and R. Magerle, *Phys. Rev. Lett.*, 2006, **97**, 016103.
- 26 R. Proksch and D. G. Yablon, *Appl. Phys. Lett.*, 2012, **100**, 073106.
- 27 Y. F. Dufrêne, D. Martínez-Martín, I. Medalsy, D. Alsteens and D. J. Müller, *Nat. Methods*, 2013, **10**, 847.
- 28 M. Krieg, G. Fläschner, D. Alsteens, B. M. Gaub, W. H. Roos, G. J. L. Wuite, H. E. Gaub, C. Gerber, Y. F. Dufrêne and D. J. Müller, *Nat. Rev. Phys.*, 2019, **1**, 41–57.
- 29 J. P. Sethna, K. Dahmen, S. Kartha, J. A. Krumhansl, B. W. Roberts and J. D. Shore, *Phys. Rev. Lett.*, 1993, **70**, 3347–3350.

- 30 G. Bertotti, *Hysteresis in Magnetism*, Academic Press, San Diego, 1998, pp. 433–477.
- 31 F. Preisach, *Z. Phys.*, 1935, **94**, 277–302.
- 32 L. Delaey, R. V. Krishnan, H. Tas and H. Warlimont, *J. Mater. Sci.*, 1974, **9**, 1521–1535.
- 33 J. Ortín, *J. Appl. Phys.*, 1992, **71**, 1454–1461.
- 34 L. Prandtl, *Z. Angew. Math. Mech.*, 1928, **8**, 85–106.
- 35 H. Lashgari, C. Tang, D. Chu and S. Li, *Comp. Mater. Sci.*, 2018, **143**, 473–479.
- 36 S. G. Gevorgian, A. E. Allahverdyan, D. S. Gevorgyan and C.-K. Hu, *Europhys. Lett.*, 2011, **95**, 23001.
- 37 R. Garcia and E. T. Herruzo, *Nat. Nanotechnol.*, 2012, **7**, 217–226.
- 38 L. Zitzler, S. Herminghaus and F. Mugele, *Phys. Rev. B*, 2002, **66**, 155436.
- 39 B. J. Briscoe, L. Fiori and E. Pelillo, *J. Phys. D: Appl. Phys.*, 1998, **31**, 2395.
- 40 W. Oliver and G. Pharr, *J. Mater. Res.*, 1992, **7**, 1564–1583.
- 41 B. Cappella and G. Dietler, *Surf. Sci. Rep.*, 1999, **34**, 1–104.
- 42 M. Dehnert and R. Magerle, *Nanoscale*, 2018, **10**, 5695–5707.
- 43 I. D. Mayergoyz, *Mathematical Models of Hysteresis*, Springer, New York, 1991.
- 44 S. Bobbio, G. Milano, C. Serpico and C. Visone, *IEEE T. Mag.*, 1997, **33**, 4417–4426.
- 45 T. Wang, M. Noori, W. A. Altabey, M. Farrokh and R. Ghiasi, *P. I. Mech. Eng. L.: J. Mat.*, 2021, **235**, 2639–2653.
- 46 A. Visintin, *Differential Models of Hysteresis*, Springer, Berlin, Heidelberg, 1994.
- 47 M. Brokate and J. Sprekels, *Hysteresis and Phase Transitions*, Springer, New York, 1996.
- 48 K. Kuhnen, *Eur. J. Control*, 2003, **9**, 407–418.
- 49 F. Moisy, *EzyFit 2.44*, MATLAB Central File Exchange, 2023.
- 50 Z. L. Shen, M. R. Dodge, H. Kahn, R. Ballarini and S. J. Eppell, *Biophys. J.*, 2010, **99**, 1986–1995.
- 51 Z. L. Shen, H. Kahn, R. Ballarini and S. Eppell, *Biophys. J.*, 2011, **100**, 3008–3015.
- 52 J. Liu, D. Das, F. Yang, A. G. Schwartz, G. M. Genin, S. Thomopoulos and I. Chasiotis, *Acta Biomater.*, 2018, **80**, 217–227.
- 53 J. A. J. v. d. Rijt, K. O. v. d. Werf, M. L. Bennink, P. J. Dijkstra and J. Feijen, *Macromol. Biosci.*, 2006, **6**, 697–702.
- 54 L. Yang, K. O. van der Werf, C. F. Fitié, M. L. Bennink, P. J. Dijkstra and J. Feijen, *Biophys. J.*, 2008, **94**, 2204–2211.
- 55 R. B. Svensson, T. Hassenkam, P. Hansen and M. S. Peter, *J. Mech. Behav. Biomed.*, 2010, **3**, 112–5.
- 56 A. Suhail, A. Banerjee and R. Rajesh, 2023.
- 57 J. Li, B. Lu, Y. Zhang, H. Zhou, G. Hu and R. Xia, *Mater. Chem. Phys.*, 2020, **241**, 122391.
- 58 H. Batzer and U. T. Kreibich, *Polym. Bull.*, 1981, **5**, 585–590.
- 59 A. V. Tobolsky, *J. Appl. Phys.*, 1956, **27**, 673–685.
- 60 A. Nicolas, E. E. Ferrero, K. Martens and J.-L. Barrat, *Reviews of Modern Physics*, 2018, **90**, 045006.
- 61 J. E. Sader, J. W. M. Chon and P. Mulvaney, *Rev. Sci. Instrum.*, 1999, **70**, 3967–3969.
- 62 C. A. Grant, M. A. Phillips and N. H. Thomson, *J. Mech. Behav. Biomed. Mater.*, 2012, **5**, 165–170.